International Journal of
Advanced Science Computing and Engineering

Journal Homepage www.ijasce.org/index.php/ijasce

Numerical Investigation of High-Temperature Thermal Energy Storage Systems Using Concrete and Nitrate Salts: Optimization and Performance Analysis

Tewodros Ayenew Eskemech [a], Natnale Sitotaw Asefa [a,*]

[a] College of Engineering and Technology, Department of Mechanical Engineering, Bonga University, Ethiopia
[b] School of Mechanical and Industrial Engineering, Addis Ababa Institute of Technology, Addis Ababa University, Addis Ababa, Ethiopia
Corresponding author: *sitotawnati2017@gmail.com

***Abstract*— This study conducts a numerical analysis of high-temperature Thermal Energy Storage (TES) systems, focusing on concrete used as a sensible heat storage material and potassium nitrate (KNO_3) as a phase change material (PCM). The study aimed to enhance the performance of TES systems in Concentrated Solar Power (CSP) plants by optimizing the number of Heat Transfer Fluid (HTF) tubes and analyzing different storage bed configurations. A 3D numerical model was developed using COMSOL Multiphysics 4.3a to simulate heat transfer processes, including fluid flow, conduction, convection, and phase change. A grid independence test ensured the accuracy of the simulations. The research identified that 25 HTF tubes provide an optimal balance between heat transfer efficiency and material usage in the nitrate salt TES model. Additionally, the cylindrical storage bed configuration reduced charging time by over 20% compared to a rectangular configuration. The results indicate that concrete can store up to 15 MJ of thermal energy, making it a viable option for CSP applications. The study also highlights the potential of embedding highly conductive materials like copper to enhance heat transfer. Recommendations for future work include exploring TES system performance under turbulent flow conditions and for intermediate temperature applications.**

***Keywords*—Thermal energy storage; optimization; heat transfer fluid; high-temperature application; COMSOL Multiphysics.**

Manuscript received 3 Dec. 2024; revised 9 Mar. 2025; accepted 6 Apr. 2025. Date of publication 30 Apr. 2025.

I. INTRODUCTION

The need for effective energy storage systems has increased due to the growing trend toward renewable energy, especially to mitigate the intermittent nature of solar electricity. One crucial technological advancement in this area is Thermal Energy Storage (TES) systems, which allow thermal energy to be captured and stored for use in situations where solar radiation is insufficient. By maintaining the supply-demand balance, TES systems not only increase the dependability of solar power but also boost the overall efficiency of energy systems [1], [2].

Applications for TES systems are numerous and include electricity generating, heating, and cooling. Their crucial importance in high-temperature applications has been brought to light by recent developments, particularly in Concentrated Solar Power (CSP) facilities where they are necessary for the production of steam [3], [4]. Sensible and latent heat storage techniques, each with unique benefits in terms of energy density and thermal stability, are commonly used in high-temperature TES systems [5], [6].

The effectiveness of TES systems depends on the use of suitable storage materials. Molten salts, especially nitrate salts, have been a popular option for high-temperature TES applications among the many materials [7]. These materials are perfect for integration with CSP technologies since they have a high energy storage density, lower vapor pressure, and stability at temperatures higher than 400°C [8], [9], [10]. The optimization of TES systems has been further investigated in recent research, with an emphasis on improving material performance and heat transfer efficiency under operating conditions [11], [12].

Therefore, the aim of this study is to conduct a comprehensive numerical analysis of the performance of TES systems designed for high-temperature applications. By developing a sophisticated 3-D Multiphysics TES model, this research explored the transient heat transfer dynamics within

these systems, to optimize their performance and advance the broader adoption of solar energy technologies.

II. Materials and Methods

A. System Description

This study focuses on a high-temperature Thermal Energy Storage (TES) system tailored for steam production in a Concentrated Solar Power (CSP) plant. The system comprises two primary cycles: the solar cycle and the power block cycle, as shown in Fig.1. The solar cycle is designed to capture and convert solar energy into thermal energy, incorporating three essential components:

1) Solar Collector: A parabolic trough collector serves as the primary component for harnessing solar energy. It concentrates sunlight onto a receiver, where the Heat Transfer Fluid (HTF) circulates, absorbing thermal energy.

2) Thermal Energy Storage (TES) Unit: A shell-and-tube TES unit is employed to store the captured thermal energy. This unit is critical for maintaining the system's ability to generate steam even during periods of low or no solar irradiation.

3) Heat Exchanger: This component transfers the thermal energy stored in the TES unit to produce saturated steam, which is crucial for power generation.

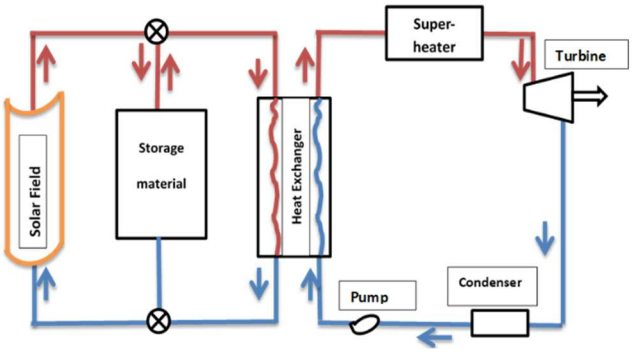

Fig. 1 TES system for high-temperature application

As Fig. 1 shows, solar radiation is collected by the parabolic trough collector, which heats the HTF circulating within the system. The heated HTF is then directed into the TES unit, where thermal energy is stored. This stored energy is subsequently utilized in the heat exchanger to generate saturated steam, after which the HTF is recirculated back to the solar collector. The power block cycle is responsible for converting the thermal energy into electricity. This process involves using the steam generated by the heat exchanger to drive a turbine. However, the scope of this study is primarily concerned with the solar cycle, particularly the performance and optimization of the TES system within the CSP framework.

The developed storage system's operation begins with the solar collector capturing and concentrating solar radiation. The heated HTF transfers thermal energy to the TES unit, where it is stored for later use. Upon entering the TES unit, this energy is stored in the selected TES material. When required, HTF releases the stored energy in the heat exchanger to produce steam, which then drives the power block cycle.

The critical function of the TES system is to store the thermal energy collected during peak solar radiation periods and release it during periods of reduced or absent solar input. This capability ensures a consistent steam supply for power generation, thereby enhancing the reliability and efficiency of the CSP plant. Material selection is paramount for optimizing TES system performance, particularly in high-temperature applications. This study investigates two materials based on their thermophysical properties and suitability for CSP systems:

4) Concrete: Selected as a sensible heat storage material due to its widespread availability, cost-effectiveness, and favorable thermal properties [13].

5) Nitrate Salt (KNO_3): Employed as a latent heat storage material, KNO_3 is chosen for its high thermal energy storage capacity, stability at elevated temperatures, and compatibility with CSP operations. Recent studies have demonstrated its effectiveness in multicomponent mixtures, optimizing melting points and thermal performance [14].

Thermal oil is utilized as the heat transfer fluid (HTF) in both cases due to its ability to operate efficiently within the required high-temperature range, with recent advancements in thermal oils further extending their operational limits and stability under extreme conditions [15]. The thermophysical properties of the selected TES materials and HTF are detailed in Table 1.

B. Sizing of the developed TES Model

The proper sizing of Thermal Energy Storage (TES) systems, particularly those utilizing concrete and nitrate salt as storage materials, is essential for achieving optimal performance in high-temperature applications. A primary focus is on the TES capacity and the rate of heat transfer, as these parameters significantly affect the required system volume and the overall cost of storage.

1) Thermo-Physical Properties:

Table 1 details the thermo-physical properties of concrete and the HTF, Therminol VP-1, which are pivotal in determining the sizing of the TES system.

TABLE I
CONCRETE TES AND HTF THERMO-PHYSICAL PROPERTIES [16]

Property	Concrete	HTF (Therminol VP-1)
Density (kg/m^3)	2200	815
Thermal conductivity (W/mK)	2	0.11
Specific heat capacity (kJ/kgK)	1.5	2.32
Temperature range (°C)	300 – 380	300 – 380

The physical model of the TES system, incorporating both concrete and nitrate salt, is designed similarly to the schematic shown in Figure 1. For this study, it is assumed that the concrete storage system is required to store thermal energy for 1.5 hours per day. The quantity of heat Q_s that needs to be stored can be estimated using Equation (2.1), with a safety factor of 1.5 applied to account for variations in the temperature of the storage material ΔT [17].

2) Design Considerations and Calculations

With a specified temperature differential ΔT of 80°C aligned with the operational temperature range of the storage material—the design parameters set the HTF tube diameter at 0.015 m and its wall thickness at 0.002 m. The storage capacity of the concrete-based TES system is determined using the following calculation:

$$Q_s = \dot{m}_f C_{pf} t(1.5\Delta T) \quad (1)$$

Where $\dot{m}_f$- HTF mass flow rate, C_{pf} - the specific heat capacity of the HTF, and t - the storage duration.

The storage material's capacity can also be expressed by Equation (2):

$$Q_s = \rho_s V_s C_{ps} \Delta T \quad (2)$$

where ρ_s -density, C_{ps} - the specific heat capacity of TES.

The total volume V_T of the storage cylinder is the sum of the concrete bed volume and the volume occupied by the HTF tubes:

$$V_T = V_S + V_t \quad (3)$$

where V_t is the volume of the shell-and-tube TES system:

$$V_t = \pi n_t {R_o}^2 L \quad (4)$$

Where n_t - the number of tubes, R_o - the outer radius of the tube, L - the length of the tubes.

The overall volume of the concrete storage cylinder is determined by:

$$V_T = \frac{\pi}{4} {D_o}^2 \quad (5)$$

where D_o - the outer diameter of the storage cylinder.

To enhance convective heat transfer in the axial direction, a length-to-diameter ratio (L/Do) of 5 is selected, in line with previous research suggesting ratios between 5 and 9 [18], [19]. For the given design, n_t =13, Ro=10 mm, and the calculated storage capacity is 15 MJ. This corresponds to an outer diameter D_o of 0.27 m and a storage bed length of 1.35 m, resulting in a total storage cylinder volume of 0.061 m³, sufficient to store the required 15 MJ of thermal energy for high-temperature applications.

C. Mathematical Modeling

1) Physical model and description:

In this study, the shell-and-tube geometric configuration was chosen for the Thermal Energy Storage (TES) bed because of its advantages, such as reduced heat loss, compact size, and high efficiency [20]. In this configuration, the storage material fills the annular space surrounding the tubes, with the HTF flowing through the tubes.

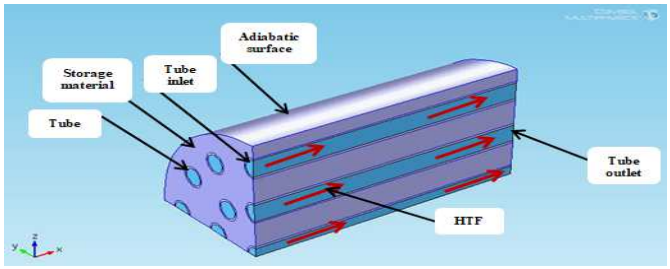

Fig. 2 A 3-D cross-sectional view of the TES bed

To optimize the computational efficiency of the simulation, one-fourth of the TES bed was modeled and analyzed. This approach significantly reduces computational time while maintaining the accuracy of the simulation results. The 3D sectional view of the shell-and-tube type TES bed is depicted in Figure 2. The simulation and analysis of the TES bed were conducted using COMSOL Multiphysics 4.3a software. This powerful tool enabled the detailed investigation of heat transfer dynamics within the TES system, providing insights into the thermal performance and efficiency of the storage bed under various operating conditions.

2) Thermal Energy Analysis of Concrete as a Storage Material:

The unit examined in this study incorporates a tube embedded within the concrete to facilitate fluid flow through the system. The HTF tubes are aligned parallel to one another along a common axis. To simplify the physical model, uniform conditions are assumed for each parallel channel, enabling the storage module to be represented as a series of sub-units, referred to as elements, arranged in parallel [21].

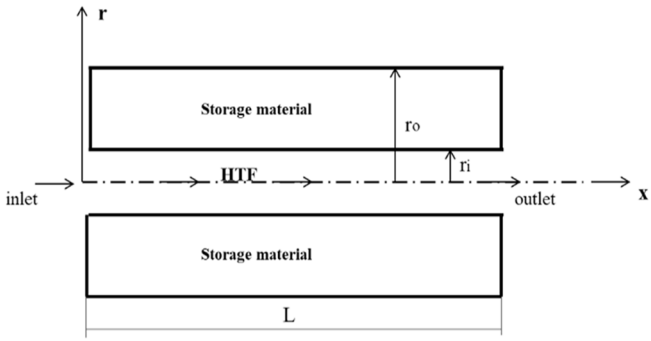

Fig. 3 TES model for one unit of concrete and HTF tubes [21]

Each element consists of a concrete-embedded cylinder with an outer radius (r_o), in contact with a tube featuring an internal radius (r_i). This configuration allows for a simplified analysis of the storage system by focusing on the behavior of a single channel. The initial section of this channel corresponds to the inlet for the HTF during the charging phase, while the final section represents the outlet during the same phase. Although the storage material surrounding the cylindrical elements is neglected in this analysis, this simplification is essential for implementing an efficient and effective thermal model [22]. This method helps in better understanding the heat transfer processes within the storage unit and supports the optimization of the TES system's performance.

D. Assumptions of the Concrete TES Model

- System geometry is axis-symmetric.
- Negligible tube thickness.
- The outer surface of the TES is insulated.
- Homogeneous TES and an isotropic process is assumed.
- Both the storage material and HTF are assumed to be at a uniform temperature throughout the system initially (T_{ini} = 573K).

1) Governing Equations:

The energy balance for the differential control volume dx of the HTF is expressed as:

$$\rho_f A_f dx \frac{\partial T_f}{\partial t} = hPdx\left(T_S - T_f\right) + \left(\dot{m}C_p\right)_f (T_{f,x} - T_{f,x+\Delta x}) \quad (6)$$

where: h is the convective heat transfer coefficient, $P = 2\pi r_i$ is the surface perimeter, and $A_f = \frac{\pi d_i^2}{4}$ is the wet area. The average fluid velocity is calculated as:

$$\bar{u} = \frac{\dot{m}_f}{\rho_f A_f} \quad (7)$$

Substituting Eq. (7) into Eq. (6) the HTF energy balance becomes:

$$\frac{\partial T_f}{\partial t} + \bar{u}\frac{\partial T_f}{\partial x} = \frac{hP}{\rho_f A_f C_{pf}}\left(T_S - T_f\right) \quad (8)$$

Similarly, with the same principle as the HTF, the energy balance for the concrete storage material can be given by [22]:

$$hPdx\left(T_s - T_f\right) = -(\rho C_p)_s A_s \frac{\partial T_s}{\partial t} \quad (9)$$

where: A_s is the cross-sectional area of the solid material. After rearranging Eq. (9) is written as:

$$\frac{\partial T_s}{\partial t} = -\frac{hPdx}{(\rho C_p)_s A_s}\left(T_s - T_f\right) \quad (10)$$

The forward finite difference method for time variation and the backward finite difference method for spatial variation are given by the following equations:

For HTF:

$$\frac{T_{f,i}^{t+\Delta t} - T_{f,i}^{t}}{\Delta t} + \bar{u}\frac{T_{f,i}^{t} - T_{f,i-1}^{t}}{\Delta x} = \frac{hP}{\rho_f A_f C_{pf}}(T_{s,i}^{t} - T_{f,i}^{t}) \quad (11)$$

For concrete storage:

$$\frac{(T_{s,i}^{t+\Delta t} - T_{s,i}^{t})}{\Delta t} = -\frac{hP}{(\rho C_p)_s A_s}(T_{s,i}^{t} - T_{f,i}^{t}) \quad (12)$$

Some rearrangement for simplification:

$$T_{s,i}^{t+\Delta t} = (1-\lambda)T_{s,i}^{t} + \lambda T_{f,i}^{t} \quad (13)$$

where:

$$\lambda = \Delta t \frac{hP}{(\rho C_p)_s A_s} \quad (14)$$

These formulations allow for the numerical solution of the governing equations by discretizing both time and space, facilitating the simulation of the heat transfer and storage dynamics in the system.

2) Initial and Boundary Conditions

It is assumed that both the Heat Transfer Fluid (HTF) and the concrete element begin at the same initial temperature.

E. Energy Analysis of Nitrate Salt (KNO_3) TES

In this investigation, a two-dimensional mathematical model was developed to analyze the energy dynamics of the nitrate salt thermal energy storage (TES) system, considering both the Heat Transfer Fluid (HTF) and the storage material [23]. The system configuration consists of an inner tube ((r_i)) to transfer the HTF, and an outer tube (r_o) that contains the nitrate salt. This setup allows efficient heat exchange between the HTF and the nitrate salt, as depicted in Fig.2.

TABLE II
NITRATE SALT (KNO3) AND THERMINOL VP-1 (HTF) THERMO-PHYSICAL PROPERTIES [8].

Property	**Nitrate salt (KNO_3)**	**HTF (Therminol VP-1)**
Density (kg/m^3)	2109 (solid)	815
Thermal conductivity (W/mK)	0.5 (liquid), 0.42 (solid)	0.11
Specific heat capacity (kJ/kgK)	0.95	2.32
Melting temperature (°C)	335	370-400
Latent heat of fusion (kJ/kg)	266	-------

1) Governing Equations:

The two-dimensional energy balance equations for the HTF and nitrate storage material can be formulated as follows, representing the fundamental heat transfer dynamics within the TES system [24], [25]:

HTF:

$$(\rho C_P)_f \pi r_i^2 \frac{\partial T_f}{\partial t} = -\left(\frac{\dot{m}}{N}C_P\right)_f \frac{dT_f}{dx} + h2\pi r_i\left(T_{r=r_i} - T_f\right) \quad (15)$$

where: N - The number of heat transfer tubes embedded in the storage bed.

Nitrate storage material:

$$\left(\rho C_p\right)_s \frac{\partial T}{\partial t} = div(k_s\, grad\, T) \quad (16)$$

The energy equation for the storage bed in differential form can be expressed as:

$$\frac{\partial}{\partial x}\left(\alpha\frac{\partial H}{\partial x}\right) + \frac{1}{r}\frac{\partial}{\partial r}\left(\alpha r\frac{\partial H}{\partial r}\right) = \frac{\partial H}{\partial t}\, dV \quad (17)$$

where:α represents the thermal diffusivity (m²/s),

- H is the enthalpy as a function of temperature, as given in Equation (16),
- r is the radial coordinate (m).

H can be calculated as a function of temperature in the phase change process as follows.

$$H(T) = \begin{cases} C_{p,s}T & T < T_{m1} \\ C_{p,l}T + \dfrac{L_F * (T - T_{m1})}{\Delta T_m} & T_{m1} \le T \le T_{m2} \\ C_{p,l}T + L_F & T > T_{m2} \end{cases} \quad (18)$$

2) Initial and boundary condition:

For the 2D numerical formulation, the following initial and boundary conditions are used.

$$t = 0: \vec{v} = 0; T_f = T = T_{ini} \quad (19\ (a))$$

$$t > 0: T(x = 0, r) = T_{inlet} \quad (19\ (b))$$

$$\frac{\partial T}{\partial x}(x = 0, r) = 0, \quad \frac{\partial T}{\partial x}(x = L, r) = 0 \quad (19\ (c))$$

$$k_s \frac{\partial T}{\partial r}(x, r = r_i) = h\left(T_{r=r_i} - T_f\right) \quad (19\ (d))$$

$$\frac{\partial T}{\partial r}(x, r = r_o) = 0 \quad (19\ (e))$$

The governing equation remains the same for both the charging and discharging processes.

HTF:

$$T_{f,i} = \frac{aT_{r=r_i} + \frac{b}{\Delta x} T_{f,i-1} + \frac{1}{\Delta t} T_{f,i}^{n-1}}{a + \frac{b}{\Delta x} + \frac{1}{\Delta t}} \quad (20)$$

where: a and b are given by the following expression;

$$a = \frac{2h}{(\rho C_p)_f r_i}, b = \frac{\dot{m}_f}{N \rho_f \pi r_i^2} \quad (21)$$

Here, h depends on whether the flow is laminar or turbulent, and it is determined using the Reynolds and Nusselt numbers [25]:

$$Re_f = \frac{2\dot{m}_f}{\pi N \mu_f r_i} \quad (22)$$

$$h = \frac{Nu_f * 2r_i}{k_f} \quad (23)$$

For laminar flow conditions, the Nusselt number is $Nu_f = 3.66$. In turbulent flow conditions, the Gnielinski correlation is applied:

$$Nu_f = \frac{\frac{f}{8}(Re_f - 1000)Pr}{1 + 12.7(f/8)^{0.5}(Pr^{2/3} - 1)}, 3000 \le Re_f \le 5 * 10^6 \quad (24)$$

The Darcy friction factor cvf is defined as:

$$(0.79 \ln Re_f - 1.64)^{-2} \quad (25)$$

3) Heat Transfer in Nitrate Salt Storage Material:

The heat transfer equation for the nitrate salt storage material is derived by applying energy conservation to a fixed control volume (i, j) with an inner radius $r_{,j-1}$ and an outer radius $r_{,j}$, as depicted in Fig. 3 [25]:

$$k_s A_i \frac{\partial T}{\partial x_i} - k_s A_{i-1} \frac{\partial T}{\partial x_{i-1}} + k_s A_j \frac{\partial T}{\partial r_j} - k_s A_{j-1} \frac{\partial T}{\partial r_{j-1}} = \rho V_{i,j} \frac{\partial H}{\partial t} \quad (26)$$

where:

$$\frac{\partial T}{\partial x_i} = \frac{T_{i+1,j}^n - T_{i,j}^n}{\Delta x}, \frac{\partial T}{\partial x_{i-1}} = \frac{T_{i,j}^n - T_{i-1,j}^n}{\Delta x} \quad (27)$$

$$\frac{\partial T}{\partial r_j} = \frac{T_{i,j+1}^n - T_{i,j}^n}{\Delta r}, \frac{\partial T}{\partial r_{j-1}} = \frac{T_{i,j}^n - T_{i,j-1}^n}{\Delta r} \quad (28)$$

$$\frac{\partial H}{\partial t_{i,j}} = \frac{H_{i,j}^n - H_{i,j}^{n-1}}{\Delta t} \quad (29)$$

Substituting the discretized expressions into the heat transfer equation gives:

$$\begin{aligned} & k_s \pi \left(r_j^2 - r_{j-1}^2\right) \frac{T_{i+1,j}^n - T_{i,j}^n}{\Delta x} - k_s \pi \left(r_j^2 - r_{j-1}^2\right) \frac{T_{i,j}^n - T_{i-1,j}^n}{\Delta x} \\ & + k_s 2\pi r_j dx \frac{T_{i,j+1}^n - T_{i,j}^n}{\Delta r} \\ & - k_s 2\pi r_{j-1} dx \frac{T_{i,j}^n - T_{i,j-1}^n}{\Delta r} \\ & = \rho \pi \left(r_j^2 - r_{j-1}^2\right) dx \frac{H_{i,j}^n - H_{i,j}^{n-1}}{\Delta t} \end{aligned} \quad (30)$$

F. Simulation and analysis of 3-D Concrete and Nitrate Salt TES Model

This section outlines the theoretical framework; governing equations, boundary and initial conditions, and the numerical formulation utilized for a three-dimensional simulation of high-temperature thermal energy storage (TES) systems. The study employs COMSOL Multiphysics 4.3a to analyze system performance. The simulation incorporates conservation principles of mass, momentum, and energy, focusing on three critical physical processes: fluid flow, heat transfer (including conduction and convection), and phase change of the storage material [26].

Continuity Equation

$$\nabla \vec{v} = 0 \quad (31)$$

Momentum Equation

$$\frac{\partial \vec{v}}{\partial t} + \rho(\vec{v}.\nabla)\vec{v} = -\nabla P + \mu \nabla^2 \vec{v} \quad (32)$$

A similar momentum equation is applied for the nitrate salt latent heat storage, maintaining the same formulation as expressed in Eq. (33) [26].

$$\begin{aligned} \rho \frac{\partial \vec{v}}{\partial t} + \rho(\vec{v}.\nabla)\vec{v} = & -\nabla P + \mu \nabla^2 \vec{v} + \rho g \beta (\mathrm{T} - T_m) \\ & + \frac{(1-\lambda)^2}{(\lambda^3 + \epsilon)} * A_{mush} * \vec{v} \end{aligned} \quad (33)$$

Energy Equation

For the Heat Transfer Fluid (HTF):

$$\rho_f * C_{p,f} * \frac{DT}{Dt} = \nabla.(k_f \nabla T_f) \quad (34)$$

For the storage material (concrete or nitrate salt):

$$\rho_s * C_{p,s} * \frac{\partial T}{\partial t} = \nabla.(k_s \nabla T_s) \quad (35)$$

Equations (34) and (35) are applied to analyze the energy dynamics in the nitrate salt storage bed and the interface between the HTF and the storage material.

G. Stored/Released Energy in the developed TES Model

The amount of heat Q, stored or released within an elemental volume of the high-temperature Thermal Energy Storage (TES) system, utilizing both sensible and latent heat storage materials, is determined using the following expression:

$$\begin{aligned} Q_{T,C} = & \rho_s * V_s * C_{ps} * (T_{inlet} - T_{ini}) + \rho_s * V_s * L_F \\ & * \lambda \end{aligned} \quad (36)$$

In this research, concrete has been chosen as the sensible heat storage material, while nitrate salt (KNO_3) is utilized as the latent heat storage material. This decision is grounded in the materials' favorable thermo-physical properties, cost-efficiency, and widespread availability [28]. Tables 2 and 3 provide a detailed summary of the thermo-physical properties of these selected materials. To assess their effectiveness for high-temperature applications, the stored energy capacity of each material is analyzed and compared. For the latent heat storage material (KNO_3), the energy stored or released is determined using the following expression:

$$Q_{T,C} = 2109 * 0.057 * 0.95 * (80) + 2109 * 0.057 * 266 = 41.1MJ$$

This calculation results in:

$$Q_{T,C} = 41.1MJ$$

This evaluation demonstrates that KNO_3 is highly effective in storing substantial amounts of energy, making it a viable candidate for high-temperature thermal energy storage applications.

H. Mesh Generation

To discretize the geometries, particularly the smaller features like the heat transfer fluid (HTF) tubes, a free tetrahedral and triangular unstructured mesh was generated. This approach allowed for a sufficient number of elements while minimizing distortion in the mesh for curved geometries [27]. The meshing process was carried out using the advanced meshing tools available in COMSOL Multiphysics 4.3a. Figure 4 illustrates the three-dimensional meshed model of the thermal energy storage bed, highlighting the detailed structure and discretization employed in the analysis.

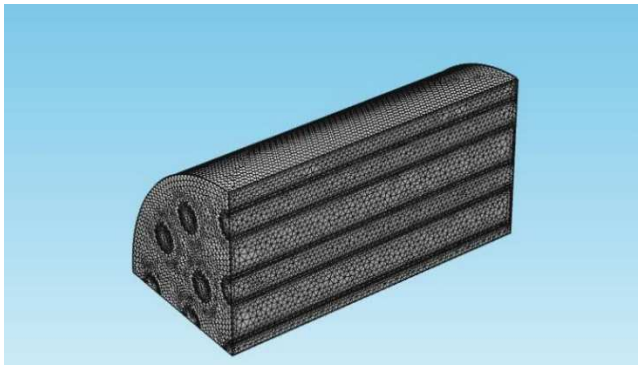

Fig. 4 The mesh generation of the developed TES model

III. Results and Discussion

A. Grid Independence Test

A grid independence test was conducted to assess the sensitivity of the numerical results from the developed mathematical model to the mesh element size. Variations in mesh element size significantly influence the numerical results across all nodes. In this study, simulations of the thermal energy storage (TES) model were performed with different mesh sizes during both the charging and discharging processes. Comparisons were made between the results obtained from various mesh densities to ensure that the outcomes were mesh-independent.

The range of mesh densities varied from 99,034 to 326,602 elements for the concrete TES model, with three distinct mesh profiles, as depicted in Fig 5. The profiles included coarse (99,034 elements), normal (199,528 elements), and fine (326,602 elements) configurations. All cases in the grid independence test commenced with the model initially set at 573 K during the charging process and 653 K during the discharging process. The results from the mesh element sizes of 199,528 and 326,602 closely aligned, as illustrated in Fig. 6.3, demonstrating a percentage reduction in element size of 43.5% between 221,624 and 125,165 elements. It is important to note that increasing the number of mesh elements resulted in a significant increase in computational time, exceeding 10 hours. Therefore, to optimize computational efficiency while maintaining accuracy, a mesh size of 199,528 elements for the concrete TES model was selected for further analysis.

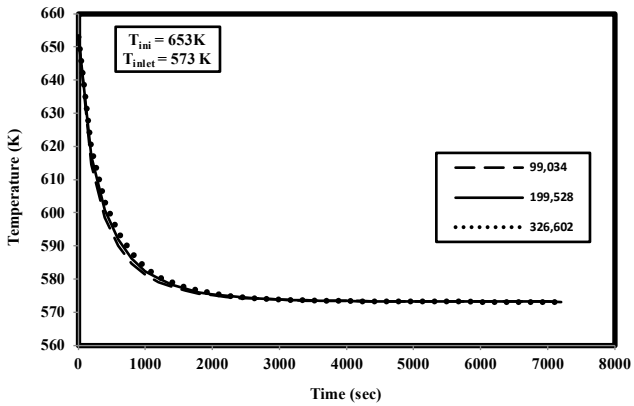

Fig. 5 Grid independent test during charging processes

B. Number of HTF Tube Optimization

The charging and discharging durations in thermal energy storage (TES) systems are notably affected by the number of heat transfer fluid (HTF) tubes used. A two-dimensional numerical model was created to assess the optimal number of HTF tubes in the TES system. The configurations examined included 13, 17, 21, 25, and 29 tubes, as shown in Fig.6. The optimization process was based on minimizing discharging time for the high-temperature TES system, while also factoring in computational time, as detailed in Table 6. For the concrete TES model, a modest decrease in discharging time (7.7%) was observed with the addition of 28 HTF tubes compared to 25 tubes. However, more substantial reductions in discharging time were seen when comparing 21 HTF tubes to 17, and 25 tubes to 21. These results indicate that fine-tuning the number of HTF tubes can significantly enhance the efficiency of the TES system.

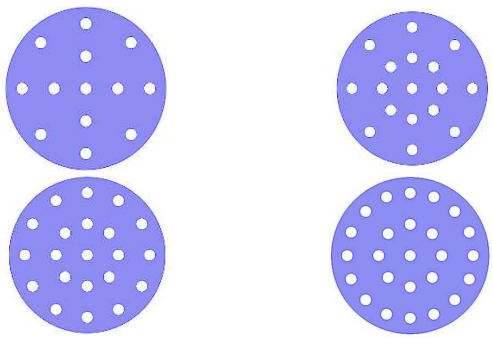

Fig. 6 Number of HTF tubes taken for optimization

TABLE III
NUMBER OF HTF TUBES OPTIMIZATION

No of HTF tubes	Discharging time (sec)	% reduction in time
17	8800	
21	7800	11.3
25	7200	7.7
29	6800	5.5

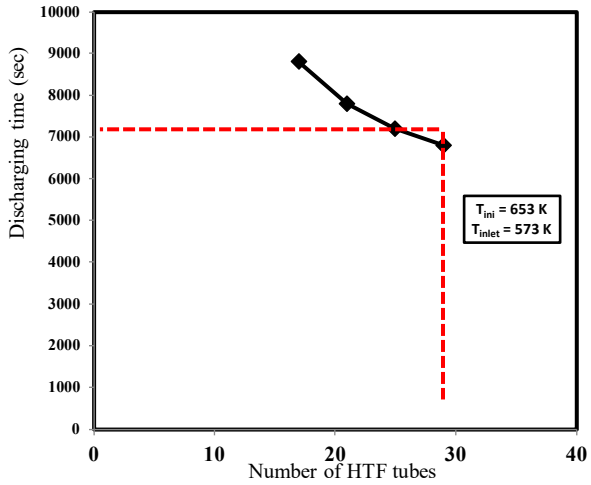

Fig. 7 Number of HTF optimizations for the concrete storage model

In this context, as shown in Fig. 7, further increasing the number of HTF tubes beyond 21 and 25 results in minimal percentage reductions in discharging time. However, this increase also incurs additional costs and reduces the effective storage volume. Consequently, for this study, 21 HTF tubes were selected for the low-temperature TES model, while 25 HTF tubes were chosen for the high-temperature TES model.

C. *Grid Independence Test*

This study performed a grid independence test in the established mathematical model to evaluate the sensitivity of the numerical findings to mesh element size. Mesh size variations can impact the model's accuracy by changing the outcomes at every computing node. In this study, simulations of the charging and discharging processes for both TES models were conducted using varying mesh densities. It was confirmed that the results were independent of grid resolution by comparing the data from these different mesh sizes. Mesh densities between 99,034 and 326,602 elements were examined for the concrete TES model utilizing three different mesh configurations at predetermined temperatures, as shown in Fig. 3. The grids in the three profiles were fine (326,602 elements), normal (199,528 elements), and coarse (99,034 elements). The model was initially set to 348 K for charging and 653 K for discharging in each model.

Figure 8 demonstrates the negligible variations between the results produced from mesh sizes of 199,528 and 326,602 elements. There was a 40% decrease in the number of elements from 369,561 to 221,624 and a 43.5% reduction from 221,624 to 125,165 elements (the first model). The second model was treated similarly. Importantly, simulations took more than ten hours to complete, indicating that higher mesh densities resulted in longer calculation times. Less than 369,561 and 326,602 mesh elements were used in the TES models to demonstrate convergence. 199,528 mesh components were used for the concrete TES model for the study's subsequent analysis to balance computational efficiency.

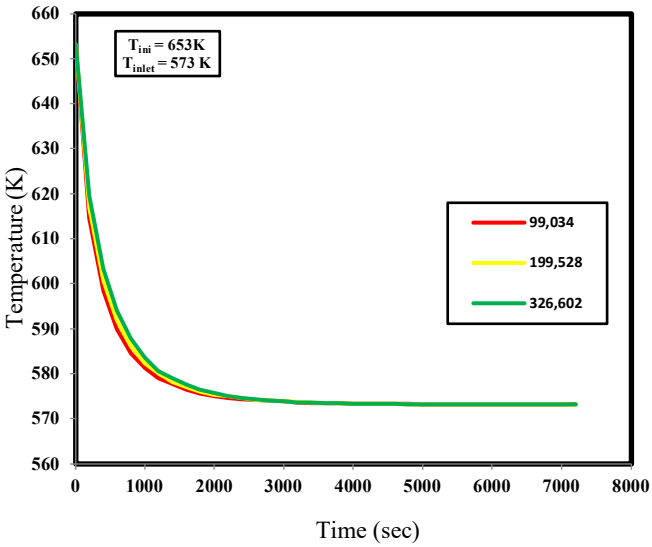

Fig. 8 Grid independent test during the charging/discharging processes

D. *Effect of TES Bed Configuration, Orientation, and Tube Arrangement*

The cylinder's orientation greatly influences the TES system's charging and discharging rates in both temperature ranges, the storage bed's geometrical design, and the tube arrangement.

1) *Geometrical Configurations:*

Using a developed 2D numerical model, this section examines the effects of various geometrical configurations of the TES bed while keeping a constant storage volume and heat transfer area. The geometrical configurations that are examined include rectangular (square) and cylindrical designs, as shown in Fig. 9. The effect of geometrical configuration is tested using a concrete-based TES model because it requires less computational time than the nitrate salt TES model.

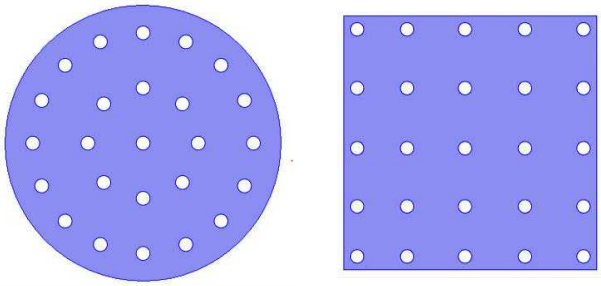

Fig. 9 Cylindrical and rectangular geometries cross-sectional view

Figure 10 shows the effect on charging time. The rectangular configuration takes 6800 seconds to charge fully, while the cylindrical configuration takes 5400 seconds. This represents a 20.58% reduction in charging time in favor of the cylindrical form. The geometry of the two configurations is the leading cause of this discrepancy. More effective heat transfer is made possible by the cylindrical bed's smooth, curved exterior. In contrast, the rectangular configuration features sharp corners and edges on the lateral faces, which hinder symmetric heat transfer. Furthermore, the more

corners and edges there are on the rectangle bed's outer edge, the longer the charging time. For these reasons, the cylindrical configuration has been selected for the present study.

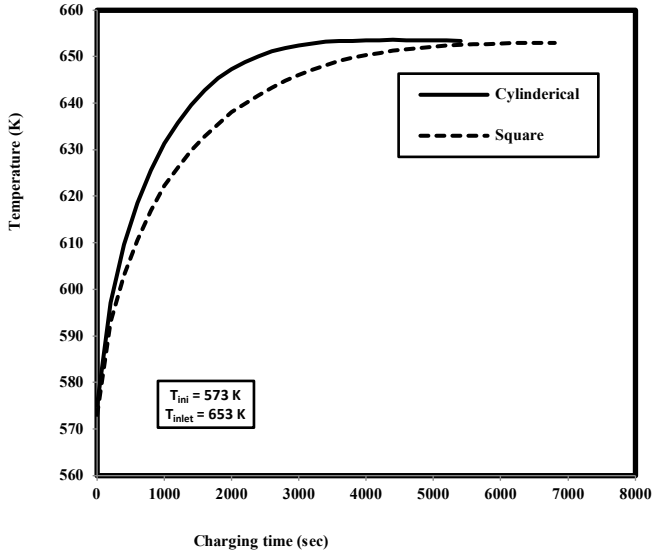

Fig. 10 Comparison of the charging time b/n the two geometries

2) Performance Parameters:

The main performance characteristics for both low-temperature and high-temperature TES models (sensible and latent) are described in this section. These factors include charging and discharging durations, energy storage or release, and the liquid fraction in the case of latent heat thermal energy storage (LHTES) beds.

3) Charging Time:

As illustrated in Fig. 11, the charging time is assessed for the two TES models created in this investigation: the nitrate salt model and the concrete model. When the volume average temperature of the storage bed is equal to the temperature of the heat transfer fluid (HTF), the bed is said to be completely charged. When the volume average temperature of the concrete storage material hits 653 K, the bed is fully charged.

4) The Charging Time:

For the concrete storage concept, the charging period for the sensible heat thermal energy storage (STES) material is 5400 seconds. The nitrate salt (KNO_3) latent heat thermal energy storage (LTES) model, on the other hand, requires 18,000 seconds to charge. The sensible heat storage material takes a lot less time to charge fully than the latent heat storage material, as seen in Fig. 11. Even when both materials occupy the same storage space, the sensible heat storage material's lower energy density than the latent heat storage material is the leading cause of this discrepancy.

5) The Discharging Time:

Fig. 12 shows the discharge time needed to release heat from the high-temperature TES models that were created, specifically the configurations of concrete and nitrate salt. When the volume's average temperature reaches the concrete storage model's starting point of 573 K, the storage bed is deemed fully discharged. For the concrete storage model, the STES material discharges in 7200 seconds, whereas the KNO_3 salt LTES model takes 19,800 seconds to discharge completely. Similar to the charging time, the discharge time for the sensible heat storage material is noticeably shorter than for the latent heat storage material, showing the higher energy density of phase change materials (PCMs) compared to sensible heat storage materials.

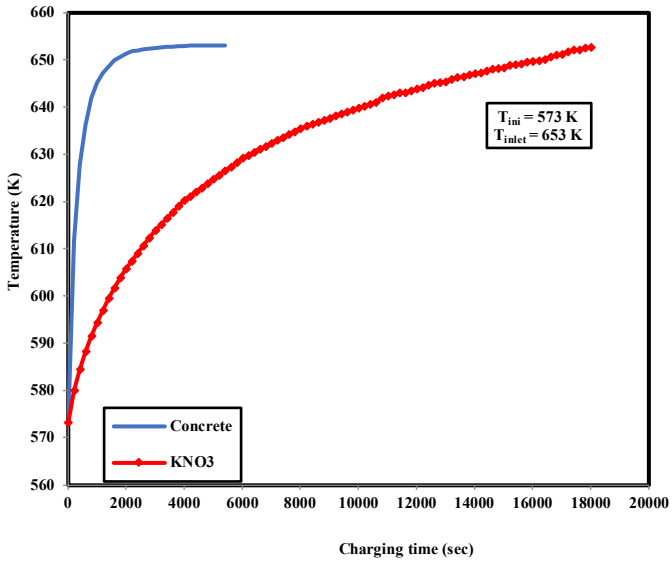

Fig. 11 Comparison b/n the charging time of SHTES and LHTES material

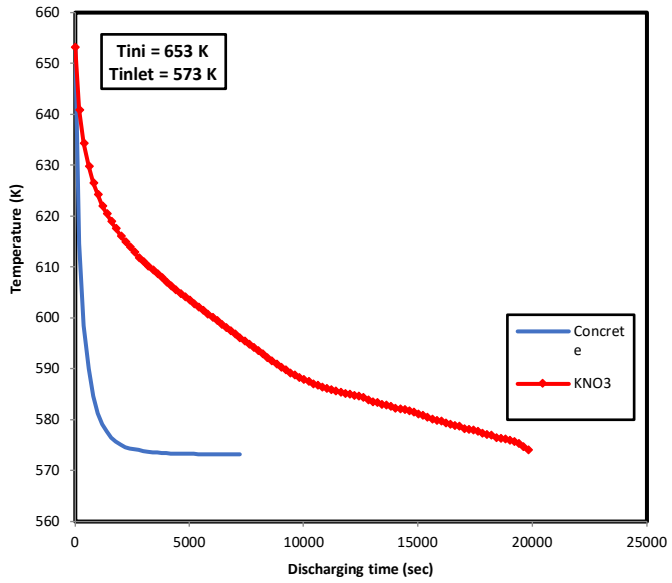

Fig. 12 Comparison b/n the discharging time of STES and LTES material

6) The Stored/Released Energy:

Over 5,400 seconds and an average temperature range of 573-653 K for concrete, the TES bed stores 15.06 MJ of sensible energy during the charging operation. Similarly, the quantity of sensible energy released from the TES bed during the discharging phase is 15 MJ, again within the 573-653 K temperature range for concrete, over 7,200 seconds.

7) The TES Model Contour Plots:

The contour map depicts the average temperature distribution of the high-temperature TES model (concrete) during the charging process. Fig. 14 depicts the temperature distribution within the concrete at various time intervals,

including 0 sec, 1200 sec, and up to 5400 sec. There is no heat transmission between the concrete storage bed and the heat transfer fluid (HTF) at t = 0 seconds. The charging process starts at the left end of the storage bed and gradually moves toward the right end, as can be seen from the contour plot. Consequently, a temperature gradient develops, with a discernible dip at the bed's right end. By the time t = 5400 sec is reached, the entire storage bed has been fully charged.

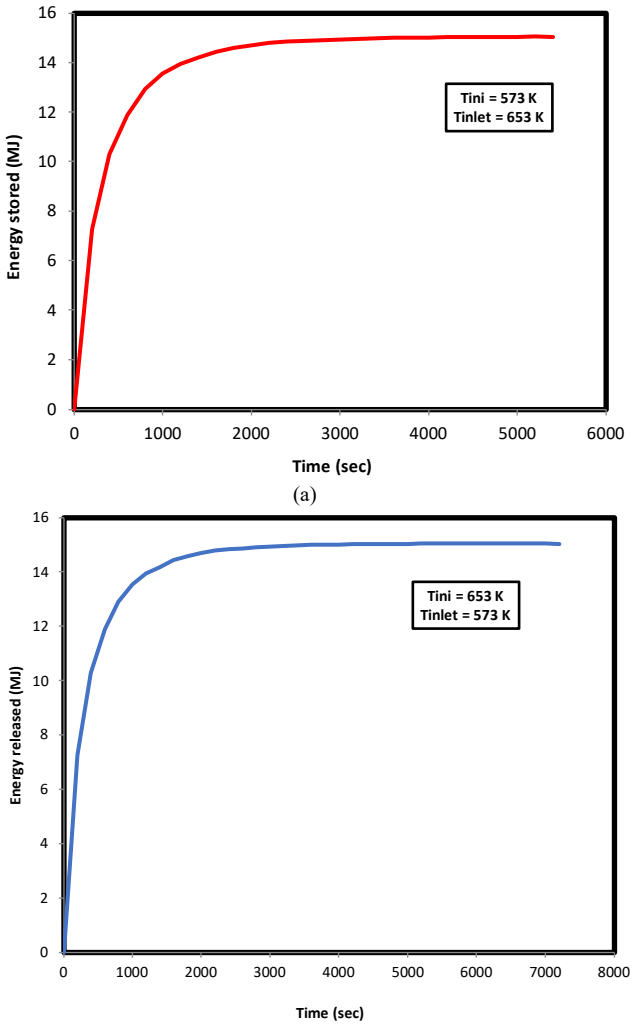

Fig. 13 Amount of energy stored/released for high-temperature TES model

8) *Average Temperature Variation of The TES Bed:*

The average temperature is determined by taking the volumetric average of all mesh elements in the numerical model. For example, the concrete TES bed starts at 573/653 K during the charging and discharging phases, and heat is transferred between the fluid and the TES material as the heat transfer fluid (HTF) flows through the HTF tubes at 573/653 K. This creates a temperature distribution, as illustrated in Fig. 15. This indicates a higher rate of heat transfer at the beginning of each process, as the temperature rises about 600 seconds during charging and falls up to 800 seconds during discharging. This behavior is explained by the higher heat transfer potential at the beginning, which diminishes over time as the temperature gradient between the HTF and the storage bed decreases.

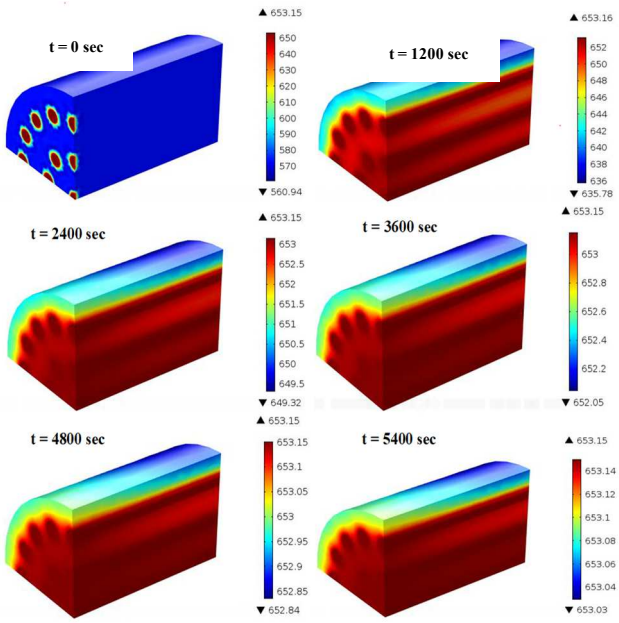

Fig. 14 The TES model Contour plots

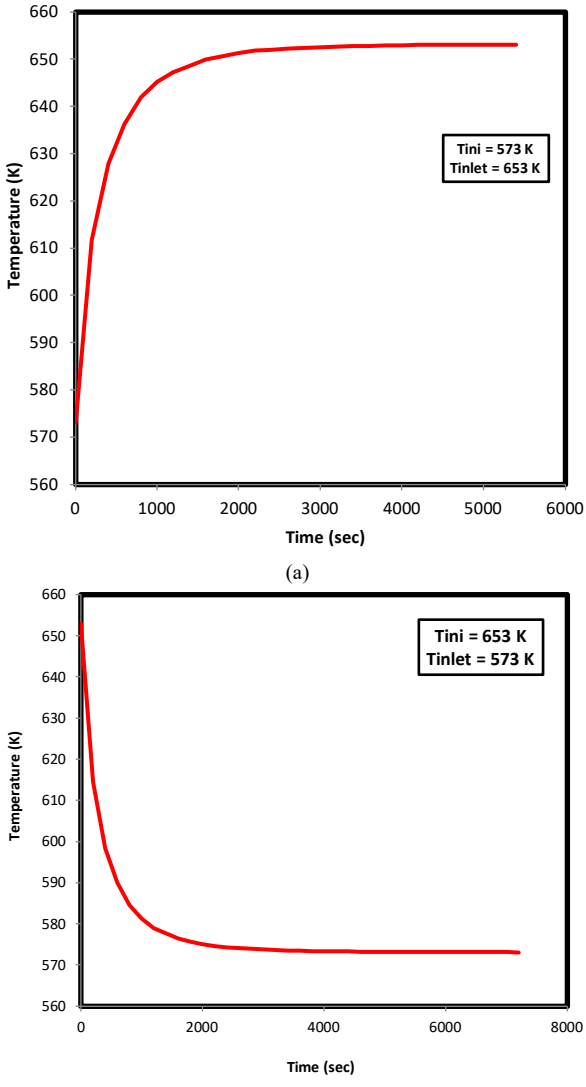

Fig. 15 Average temperature variation curve during the charging / discharging processes

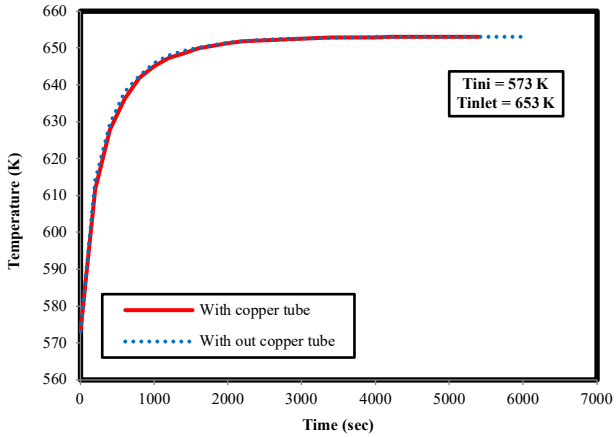

Fig. 16 Heat transfer enhancement technique for SHTES model

9) *Validation of the Present TES Model*

This study was validated by contrasting it with comparable numerical and experimental research carried out by other writers, including [29], [30]. The validation results reveal that the numerical model created in this study agrees well with the experimental and numerical results from the cited papers, notwithstanding this discrepancy.

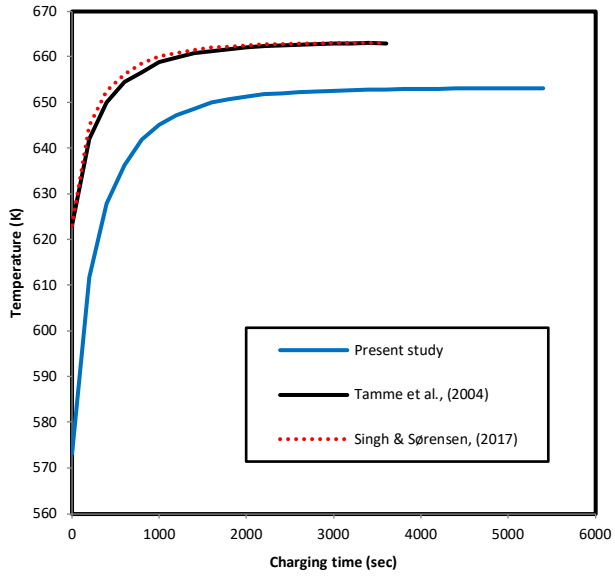

Fig. 17 Model validation for SHTES model during the charging process

IV. Conclusion

Key performance parameters, such as charging/discharging time and energy stored/released, were evaluated for both developed TES models. A heat transfer enhancement technique was implemented, involving the insertion of copper tubes between concrete storage beds and the use of multiple HTF tubes, to reduce charging time. This three-dimensional numerical model successfully simulated the behavior of heat transfer fluid (HTF) flow and heat transfer within a sensible storage material (concrete), addressing the conjugate heat transfer problem. The governing equations for the TES model were solved using the commercial program COMSOL Multiphysics 4.3a. The results of the model were validated against both experimental data and previous numerical studies, showing strong agreement.

The following is a summary of the study's key findings: The model showed that employing concrete as a storage material might retain 15 MJ of heat energy for high-temperature applications, like steam generation in concentrating solar power (CSP) facilities. Following the HTF tube optimization procedure, an ideal setup was found, suggesting the usage of 25 HTF tubes for both paraffin and concrete TES models. For the concrete TES model, the charging and discharging times were found to be 5,400 and 7,200 seconds, respectively. Conduction dominated the heat transfer during discharging, whereas convection was more critical during charging, which is why discharge happened more slowly than charging. It was discovered that the charging and discharging times were significantly impacted by the inlet HTF temperature. Furthermore, a multi-HTF tube arrangement inside the storage bed and the addition of a highly conductive metal, like copper, worked well to increase the rate of heat transfer, resulting in a 13% decrease in the charging time for the concrete storage model.

There are several directions for further investigation, even though the focus of this work was on evaluating the TES system's effectiveness across several parameters. Although the primary focus of this analysis was on high-temperature applications, future research might examine how well TES systems operate in intermediate temperature ranges to assess their potential for other applications. A laminar flow regime with a modest HTF flow rate was used in the current investigation. This might be expanded in future research by looking at a turbulent flow regime, which could offer advantages including higher heat transfer rates and better system performance.

Reference

[1] M. Mubarrat *et al.*, "Research advancement and potential prospects of thermal energy storage in concentrated solar power application," *Int. J. Thermofluids*, vol. 20, p. 100431, Nov. 2023, doi:10.1016/j.ijft.2023.100431.

[2] M. Ibarra *et al.*, "Advances in thermal energy storage systems: A review," *Renew. Sustain. Energy Rev.*, vol. 134, p. 110358, 2020.

[3] L. Cirocco *et al.*, "Thermal energy storage for industrial thermal loads and electricity demand side management," *Energy Convers. Manage.*, vol. 270, p. 116190, Oct. 2022, doi:10.1016/j.enconman.2022.116190.

[4] O. Achkari and A. El Fadar, "Latest developments on TES and CSP technologies—Energy and environmental issues, applications and research trends," *Appl. Therm. Eng.*, vol. 167, p. 114806, Feb. 2020, doi: 10.1016/j.applthermaleng.2019.114806.

[5] Y. Jiang, M. Liu, and Y. Sun, "Review on the development of high temperature phase change material composites for solar thermal energy storage," *Sol. Energy Mater. Sol. Cells*, vol. 203, p. 110164, Dec. 2019, doi: 10.1016/j.solmat.2019.110164.

[6] R. Kumar *et al.*, "Application of phase change material in thermal energy storage systems," *Mater. Today: Proc.*, vol. 63, pp. 798–804, 2022, doi: 10.1016/j.matpr.2022.06.152.

[7] F. Alnaimat and Y. Rashid, "Thermal energy storage in solar power plants: A review of the materials, associated limitations, and proposed solutions," *Energies*, vol. 12, no. 21, p. 4164, Oct. 2019, doi:10.3390/en12214164.

[8] M. Maaza, "Latent and thermal energy storage enhancement of silver nanowires–nitrate molten salt for concentrated solar power," *J. Energy Storage*, vol. 30, p. 101532, 2020.

[9] E. González-Roubaud, D. Pérez-Osorio, and C. Prieto, "Review of commercial thermal energy storage in concentrated solar power plants: Steam vs. molten salts," *Renew. Sustain. Energy Rev.*, vol. 80, pp. 133–148, Dec. 2017, doi: 10.1016/j.rser.2017.05.084.

[10] A. Boretti and S. Castelletto, "High-temperature molten-salt thermal energy storage and advanced-ultra-supercritical power cycles," *J. Energy Storage*, vol. 42, p. 103143, Oct. 2021, doi:10.1016/j.est.2021.103143.

[11] A. K. Kumar *et al.*, "Recent advances in thermal energy storage with phase change materials and molten salts for solar energy applications: A state-of-the-art review," *J. Energy Storage*, vol. 42, p. 103066, 2021.

[12] D. S. Jayathunga *et al.*, "Phase change material (PCM) candidates for latent heat thermal energy storage (LHTES) in concentrated solar power (CSP) based thermal applications—A review," *Renew. Sustain. Energy Rev.*, vol. 189, p. 113904, Jan. 2024, doi:10.1016/j.rser.2023.113904.

[13] X. Fang *et al.*, "Saturated flow boiling heat transfer: Review and assessment of prediction methods," *Heat Mass Transf.*, vol. 55, no. 1, pp. 197–222, Aug. 2018, doi: 10.1007/s00231-018-2432-1.

[14] Q. Yu *et al.*, "Comprehensive thermal properties of molten salt nanocomposite materials base on mixed nitrate salts with SiO_2/TiO_2 nanoparticles for thermal energy storage," *Sol. Energy Mater. Sol. Cells*, vol. 230, p. 111215, Sep. 2021, doi:10.1016/j.solmat.2021.111215.

[15] M. Kenisarin *et al.*, "High-temperature phase change materials for thermal energy storage," *Renew. Sustain. Energy Rev.*, vol. 103, pp. 83–95, 2020.

[16] M. Barrasso *et al.*, "Latest advances in thermal energy storage for solar plants," *Processes*, vol. 11, no. 6, p. 1832, Jun. 2023, doi:10.3390/pr11061832.

[17] H. Niyas, C. R. C. Rao, and P. Muthukumar, "Performance investigation of a lab-scale latent heat storage prototype—Experimental results," *Sol. Energy*, vol. 155, pp. 971–984, Oct. 2017, doi: 10.1016/j.solener.2017.07.044.

[18] G. Rekkas Ventiris, "Archimede concentrated solar power plant dynamic simulation: Control systems, heat transfer fluids and thermal energy storage," *Energy Rep.*, vol. 7, pp. 123–135, 2021.

[19] A. Gautam and R. P. Saini, "A review on technical, applications and economic aspect of packed bed solar thermal energy storage system," *J. Energy Storage*, vol. 27, p. 101046, Feb. 2020, doi:10.1016/j.est.2019.101046.

[20] Q. Mao, "Recent developments in geometrical configurations of thermal energy storage for concentrating solar power plant," *Renew. Sustain. Energy Rev.*, vol. 59, pp. 320–327, Jun. 2016, doi:10.1016/j.rser.2015.12.355.

[21] Y. Jian *et al.*, "Design and optimization of solid thermal energy storage modules for solar thermal power plant applications," *Appl. Energy*, vol. 139, pp. 30–42, Feb. 2015, doi: 10.1016/j.apenergy.2014.11.019.

[22] J. Raccanello, S. Rech, and A. Lazzaretto, "Simplified dynamic modeling of single-tank thermal energy storage systems," *Energy*, vol. 182, pp. 1154–1172, Sep. 2019, doi: 10.1016/j.energy.2019.06.088.

[23] Y. Qiao *et al.*, "Experimental study of thermo-physical characteristics of molten nitrate salts based nanofluids for thermal energy storage," *ES Energy Environ.*, vol. 4, no. 3, pp. 48–58, 2019.

[24] A. Palacios *et al.*, "Thermal energy storage technologies for concentrated solar power—A review from a materials perspective," *Renew. Energy*, vol. 156, pp. 1244–1265, Aug. 2020, doi:10.1016/j.renene.2019.10.127.

[25] T. Esence *et al.*, "A review on experience feedback and numerical modeling of packed-bed thermal energy storage systems," *Sol. Energy*, vol. 153, pp. 628–654, Sep. 2017, doi: 10.1016/j.solener.2017.03.032.

[26] U. M. Jad and A. P. Shah, "Numerical analysis on thermal energy storage tank filled with phase change material," *JNX*, vol. 4, no. 5, pp. 303–307, 2018.

[27] L. Prasad and P. Muthukumar, "Design and optimization of lab-scale sensible heat storage prototype for solar thermal power plant application," *Sol. Energy*, vol. 97, pp. 217–229, Nov. 2013, doi:10.1016/j.solener.2013.08.022.

[28] G. Alva, Y. Lin, and G. Fang, "An overview of thermal energy storage systems," *Energy*, vol. 144, pp. 341–378, Feb. 2018, doi:10.1016/j.energy.2017.12.037.

[29] D. Laing *et al.*, "Solid media thermal storage for parabolic trough power plants," *Sol. Energy*, vol. 80, no. 10, pp. 1283–1289, Oct. 2006, doi: 10.1016/j.solener.2006.06.003.

[30] M. Singh and B. Sørensen, "A simplified approach for modeling thermal energy storage systems in concentrated solar power applications," *Energy*, vol. 112, pp. 181–193, 2017.

[31] G. J. W. Kathrine *et al.*, "Variants of phishing attacks and their detection techniques," in *Proc. 3rd Int. Conf. Trends Electron. Inform. (ICOEI)*, Apr. 2019, pp. 255–259, doi: 10.1109/icoei.2019.8862697.